Measurement of ^{208}Pb$(n,\gamma)^{209}$Pb Maxwellian averaged neutron capture cross section

L. Weissman,[1,*] M. Tessler,[2] A. Arenshtam,[1] I. Eliyahu,[1] S. Halfon,[1] C. Guerrero,[3] B. Kaizer,[1] D. Kijel,[1] A. Kreisel,[1]
T. Palchan,[2] M. Paul,[2] A. Perry,[1] G. Schimel,[1] I. Silverman,[1] A. Shor,[1] N. Tamim,[1] and S. Vaintraub[1]

[1]*Soreq Nuclear Research Center, Yavne 81800, Israel*
[2]*Racah Institute of Physics, Hebrew University, Jerusalem 91904, Israel*
[3]*Universidad de Sevilla, 41012 Seville, Spain*

The doubly magic ^{208}Pb nucleus is a bottleneck at the termination of the *s*-process path due to its very low neutron capture cross section. This cross section is also important for the decomposition of *s*, *r* processes and U/Th radiogenic decay contributions to the Pb-Bi solar abundances. The ^{208}Pb$(n,\gamma)^{209}$Pb cross section was measured at the Soreq Applied Research Accelerator Facility Phase I using an intense quasi-Maxwellian neutron source produced by irradiation of the liquid-lithium target with a 1.5-mA continuous-wave proton beam at 1.94 MeV. The cross section was measured by counting the β activity from the irradiated lead target. The measurement allowed us to evaluate the Maxwellian averaged cross section (MACS) at 30 keV obtaining a value of 0.33(2) mb. This has been compared with the earlier activation and time-of-flight measurements found in the literature. The MACS cross-sectional value of the ^{63}Cu$(n,\gamma)^{64}$Cu reaction was determined in the same experiment and is compared to a recent published value.

I. INTRODUCTION

The ^{208}Pb nucleus has the lowest neutron capture cross section among the heavy nuclides ($A > 56$) in the astrophysical neutron energy range of $kT \sim 30$ keV. Therefore ^{208}Pb acts as an extreme bottleneck for the reaction flow at the termination of the *s* process in ^{209}Bi, the last stable *s*-process isotope. Both *s* and *r* processes as well as the U and Th decays contribute to the complex abundance patterns of Pb and Bi abundances, which have been the subject of numerous investigations. In this context, it is desirable to know the ^{208}Pb(n,γ) cross-sectional value to an accuracy of $\sim$3% [1]. Furthermore, the large discrepancy between calculated and observable abundances of ^{208}Pb and ^{209}Bi isotopes led to the suggestion of a strong component of the *s* process [2]. Later on this discrepancy was understood in terms of a contribution of a broad range of stars, including low metallicity ones into abundances of these isotopes [3]. The latter stars have higher numbers of free neutrons per iron seeds which results in abundance distribution shifting towards heavy elements [4]. Accurate knowledge of the ^{208}Pb$(n,\gamma)^{209}$Pb cross section is important for the decomposition of these different contributions [5].

The precise measurement of such a low cross-sectional reaction presents a serious experimental challenge. Extensive time-of-flight (TOF) measurements were performed at the GELINA accelerator [6]. However, a significant part of the ^{208}Pb(n,γ) reaction rate is due to the direct capture (DC) mechanism which is very difficult to estimate in TOF measurements. Thus, a theoretical calculation of the DC contribution in the ^{208}Pb$(n,\gamma)^{209}$Pb cross section has been used in Ref. [6]. With activation measurements, both the DC and the resonance contributions are measured simultaneously.

The ^{7}Li$(p,n)^{7}$Be reaction at proton energy just above the reaction threshold of 1.880 keV has been used for many years

for activation measurements with neutron fluxes having an energy distribution similar to a Maxwellian distribution at $kT \sim 25$ keV [7]. These measurements yield a direct estimation of the Maxwellian averaged cross section (MACS) needed for the calculation of stellar reaction rates. Such activation measurements of the ^{208}Pb$(n,\gamma)^{209}$Pb cross section were performed at the 3.7-MeV Karlsruhe Van de Graaff accelerator [5,8]. It is worthwhile to mention that the β decay of ^{209}Pb takes place without emission of delayed γ rays, which is a major challenge compared to typical activation experiments.

Recently the high-power liquid-lithium target (LiLiT) [9,10] has been built and commissioned at Phase I of the Soreq Applied Research Accelerator Facility (SARAF) [11]. Bombardment of LiLiT by 1 to 2 mA Continuous Wave (CW) proton beams allows one to obtain a quasi-Maxwellian neutron source more intense by a factor $\sim$50 than that used in the previous experiments [8]. The experimental astrophysical program at SARAF includes measurements of the weakest (n,γ) cross sections on ^{208}Pb and ^{209}Bi isotopes which take place at the termination of the *s*-process path. In this paper we report on a new measurement of the ^{208}Pb$(n,\gamma)^{209}$Pb cross section performed at SARAF. A measurement of the ^{209}Bi$(n,\gamma)^{210g,m}$Bi cross section will be reported separately.

II. IRRADIATION

Details on LiLiT and its irradiation procedure were published in Refs. [9,10,12] and references therein. The target is an 18-mm-wide and 1.5-mm-thick windowless liquid-lithium film at $\sim$200 °C, forced flown at a speed of a few meters per second by an electromagnetic pump. The lithium film is supported by a stainless-steel wall. As demonstrated during the LiLiT commissioning, the target can operate with stable flow, vacuum, temperature, and radiation conditions while dissipating $\sim$3 kW of proton beam power and can be used as a neutron-producing source.

*weissman@soreq.gov.il

015802-1

A 25 × 25 mm^2 self-supporting lead foil of chemical purity better than 99.99% was used as an activation target. According to the manufacturer [13] the nominal thickness of the foil was 3 μm. The average thickness was independently determined by weighing to be 3.79(2) mg/cm^2 [3.34(2) μm]. The lead foil was sandwiched between two 25 × 25 mm^2 gold foils, and the neutron fluence was determined from the ^{198}Au activity using the ^{197}Au$(n,\gamma)^{198}$Au cross section which is well established in a broad energy range [14,15]. Furthermore, γ autoradiography of the activated gold foils allows one to determine the relative position of the neutron cone with respect to the target assembly. The thickness values of the gold foils were determined by weighting and found to be 23.6(1) and 23.4(1) mg/cm^2 for upstream and downstream foils, respectively. In addition, a thin 25 × 25 mm^2 copper foil was placed between the lead and the downstream gold foil. This foil was used for subsequent determination of the efficiency of a β detector used in the measurements (see below). The copper layer was supported by a 12.5-μm-thick Mylar sheet [16]. The Monte Carlo simulations (see below) confirmed that the effect of the Mylar layer on both neutron absorption and scattering was negligible. The thickness of the copper layer was measured by Rutherford backscattering (RBS) with a 3-MeV He$^+$ beam at the Bar-Ilan Ion Beam Analysis Laboratory and was found to be 1.31(1) × 10^{18} at/cm^2. The four foils were aligned carefully, pressed together, and placed at the irradiation position 6-mm downstream of the surface of the lithium film [12].

The SARAF accelerator[1] was tuned using a pilot proton beam of 1.5-mA peak intensity and a low duty cycle of 0.5%. The beam duty cycle was defined using the SARAF slow chopper [17]. Only three cavities were used for acceleration, whereas the other three cavities were idle and detuned. Protons scattered off a 50-μg/cm^2 gold foil evaporated on a thin carbon layer were detected by a silicon detector which was calibrated *in situ* by ^{228}Th and ^{148}Gd α sources. The energy of the scattered protons corrected for the RBS kinematic factor and for energy loss in the gold target yielded the beam energy. The beam energy was tuned to be 1938(3) keV with an energy spread of 15 keV (1σ). After energy tuning the pilot beam was transported along the beam line and tuned on the LiLiT target using two Faraday cups, four wire profilers, a current reading from collimators, as well as the temperature reading on the LiLiT side plates [9,17]. The proton current on the lithium was calibrated at a 5% duty cycle using neutron counting measured by a ^{235}U fission chamber placed downstream of the target. A Faraday cup located 1 m upstream from the target was used for current calibration. In addition γ radiation counters and a neutron dosimeter were used for monitoring the beam intensity [10], and the temperature reading on the side plates of the LiLiT nozzle were used for fine beam adjustment during the run [17]. After the tune, the beam duty cycle was ramped up to 99%. Normally the first ramp up is performed rather slowly (20–30 min) while monitoring the temperature and radiation along the beam line and the target and applying fine-tuning on the beam-line magnet currents. The following
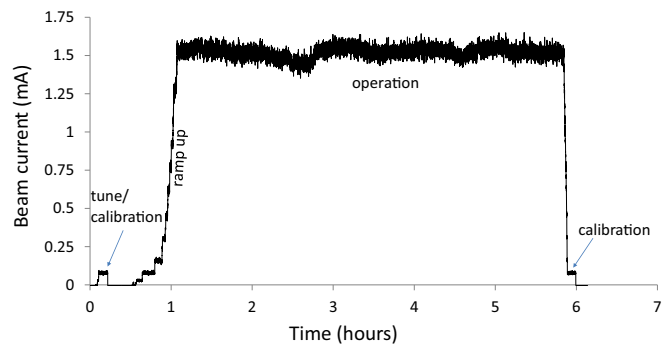

FIG. 1. Beam logarithm during the irradiation. The counting rate of a fission chamber is used as a beam current monitor (see Refs. [10,12] for details).

beam rampings, if irradiation is stopped due to an accelerator problem or an experimental requirement, are performed much faster ($\sim$5 min). After the ramping up procedure the current was kept on the target during approximately 5 h which is compatible with the ^{209}Pb half-life (3.253 h). The beam was stable within ±5% (see Fig. 1); the small beam current variation with time is due to the instability of the ion source. The calibration of the fission chamber rate against the current reading at the Faraday cup was verified again upon the end of irradiation. The total beam charge collected on the target was 27(1) C (7.51 mA × h). The uncertainty in the estimation of the collected beam charge does not contribute to the total uncertainty of the measured cross section, which is based on the measured activity of the Au and Cu foils (Table II below).

III. ACTIVITY MEASUREMENTS

The samples were taken out of the irradiation setup and brought to the counting laboratory as soon as the radiation level allowed for entrance to the hall ($\sim$15 min). Two detectors were available for counting γ and β activities, respectively: a shielded 25% relative efficiency high-purity Ge detector from Ortec and a β counter iSolo500 from Canberra [18]. The latter counter has a 500-mm^2 area and a 500-μm-thick passivated implanted planar silicon detector. The iSolo counter, its electronics, and data acquisition are commercial instruments, which do not allow for any modification by the user. As a first step to identify potential contaminants that could affect the β measurements, a γ spectrum of the lead foil was measured by placing it in contact with a HPGe detector for a period of 30 min [Fig. 2(a)]. No shielding was placed between the target and the detector. One can observe in the spectrum weak γ rays from ^{24}Na as well as two weak unknown 388- and 232-keV γ rays. The two latter transitions were not observed in a spectrum taken a few hours later. We cannot comment on the origin of either of these transitions, but their weak intensity indicates a lack of significant contaminants in the irradiated foil. Next, the lead target was taken to the β counter, and β activity was measured for 15 h. The accumulated β spectrum was saved and reset automatically every 15 min. Dependence of the β activity as a function of time together with the fit function is shown in Fig. 2(b). The used fitting function is $f(t/\tau) =$

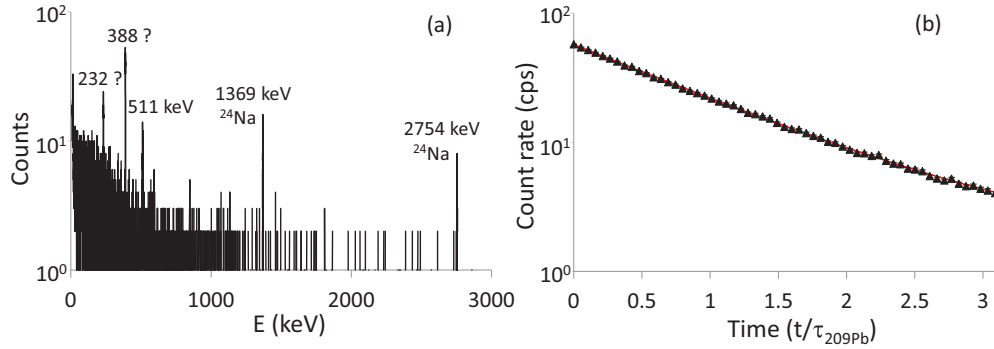FIG. 2. (a) The γ spectrum of the lead foil taken in contact with the Ge detector immediately after irradiation. (b) The β counting rate of the lead sample as a function of time together with the fitting curve. Time is presented in ^{209}Pb mean lifetime units.

$a \exp(-bt/\tau) + c$, where τ is the ^{209}Pb mean decay time. The fit yielded the value of the b parameter of 1.001(15) indicating that the β particles from the foil are only from the ^{209}Pb decay. The possible contribution of ^{24}Na in the decay curve is negligible within uncertainties of the fitting parameters.

The detection efficiency of the Ge detector as a function of γ energy and the distance to the source was measured to an accuracy of $2.5\% - 3\%$ using a set of calibrated γ sources. The detection efficiency of the iSolo500 detector is a more complicated issue. Preliminary energy calibration of the iSolo β detector was performed with ^{228}Th, ^{148}Gd, and ^{241}Am α sources and with a ^{207}Bi electron source (emitting conversion electrons with a dominant monoenergetic component at 976 keV). A calibrated α source was used to evaluate the solid angle of the detector from the sample position. Owing to the relatively high-energy threshold of the detector ($\sim$125 keV) [18], the calibration was checked carefully using β particles emitted by the activated Cu and Au foils of known activity from the γ measurements. The properties of the three isotopes produced during the activation are shown in Table I. The ^{209}Pb nucleus emits only β particles with a rather low-energy end point of 644 keV. Therefore, accuracy of the ^{209}Pb β activity measurement strongly depends on the low-energy β counter threshold and the corresponding uncertainty in the detection efficiency. Decay of the ^{64}Cu nucleus has been measured very accurately as this isotope is used for neutron flux dosimetry in nuclear reactors as well as for positron emission tomography imaging [19]. The end points from ^{64}Cu decay are 579 and 655 keV for β^+ and β^- decays correspondingly, close to that of ^{209}Pb. A weak 1345.8-keV γ ray in ^{64}Cu decay allows one to compare the β and γ counting rates and, hence, to determine the efficiency of the iSolo counter for a β energy distribution similar to that of ^{209}Pb.

The β energy spectra from the lead and copper foils are compared in Fig. 3. The copper foil spectrum (diamonds) was taken immediately after irradiation for a duration of 30 min, whereas the lead foil spectrum (circles) was collected during 15 h. A background spectrum collected for 25 h was subtracted from the spectra in Fig. 3 with the corresponding normalization factor. The ratio of integrals of the background and ^{209}Pb sample spectra is less than 2%. The contribution of the β background into the statistical error is considered as negligible. As seen in Fig. 3, the spectra from the two isotopes are basically identical except for a weak high-energy tail of negligible intensity. This observation supports the assumption that the ^{64}Cu isotope can be used reliably for calibration of the β counter efficiency. The β spectrum from the gold sample also is shown in Fig. 3.

A γ spectrum of the copper sample is shown in Fig. 4(a). The spectrum was taken at 5-cm distance from the Ge detector to maximize counting in the weak 1345.8-keV peak. The detection efficiency at this energy and distance is 0.419(11) %. This Ge efficiency value was corrected by a factor of 1.04(1) associated with geometrical parameters of the copper sample. This factor was obtained using the GESPECOR software [20]. The ratio of the background subtracted β particles integral from the copper sample to the integral of the 1345.8-keV γ peak corrected for the Ge detector efficiency, γ, β, and positron branching ratios, and decay losses yield the β counter efficiency. The obtained efficiency value $\varepsilon_{^{64}\mathrm{Cu}}$ is 25.6(1.2)%. The main contribution in the experimental uncertainty is due to the statistical error of the 1345.8-keV peak integral. The 511-keV γ rays from positrons' annihilation [Fig. 4(a)] were not used for the determination of ^{64}Cu activity due to nonreliable knowledge on their geometrical origin. The β efficiency value was confirmed in separate γ and β measurements of a copper

TABLE I. Properties of the produced isotopes are presented. The quoted values of the experimental and simulated β detection efficiencies are explained in the text.

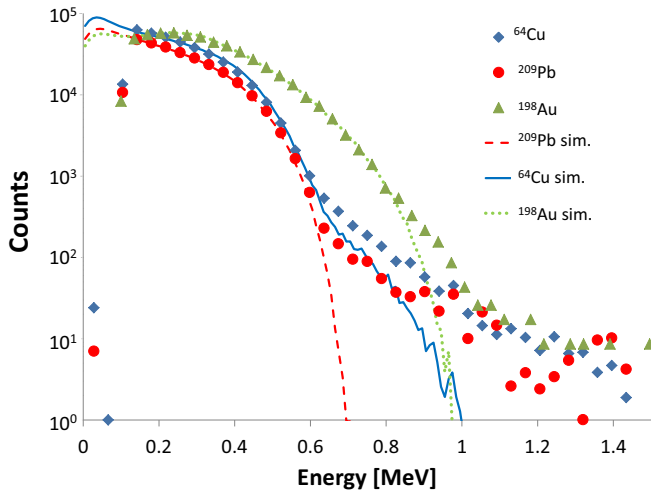| Isotope	Half-life (h)	Decay	Decay branching (%)	End point (keV)	γ energy/branch (keV)/(%)	Expt. efficiency (%)	Simulated efficiency (%)
^{209}Pb	3.253	β^-	100	644	None	25.6 (1.2)	20.7(10)
^{64}Cu	12.70	β^-/β^+	38.5(3)/17.5(2)	579/655	1345.8/0.475(3)		21.2(10)
^{198}Au	64.68	β^-	100	961	411.8/95.6(1)	28.2(6)	24.2(10)

FIG. 3. Experimental β spectra taken from ^{64}Cu (diamonds), ^{209}Pb (circles), and ^{198}Au (triangles) are compared with the results of the GEANT simulations. The experimental spectra and simulations are normalized by arbitrary factors to reduce the density of the figure.

foil sample activated at the Soreq research reactor. The sample was active enough to achieve a good counting statistics (better than a 1% statistical error) for the 1345.8-keV transition at the distance of 40 cm from the Ge detector.

For completeness, the β counter efficiency also was measured for the ^{198}Au gold samples. An arbitrary normalized β energy spectrum from one of the gold foils is shown in Fig. 3. The γ spectrum taken from one of the gold foils a day after irradiation is shown in Fig 4(b). The spectrum was taken at 40-cm distance from detector during 10 min. The detection efficiency of 411.8 keV at this distance was 0.041(1)%. Both upstream and downstream gold foils yielded γ activities of 1.026×10^5 and 1.014×10^5 counts indicating negligible neutron scattering within the target foil stack. Comparison of the measured β activity with an intensity of 411.8 keV corrected by the Ge detector efficiency, branching ratio, and decay losses yields the β detection efficiency. This value is determined as $\varepsilon_{^{198}\text{Au}} = 28.2(6)\%$. The probability of emission of conversion electrons [4.39(7)%] from deexcitation of the 411.8-keV level was taken into account.
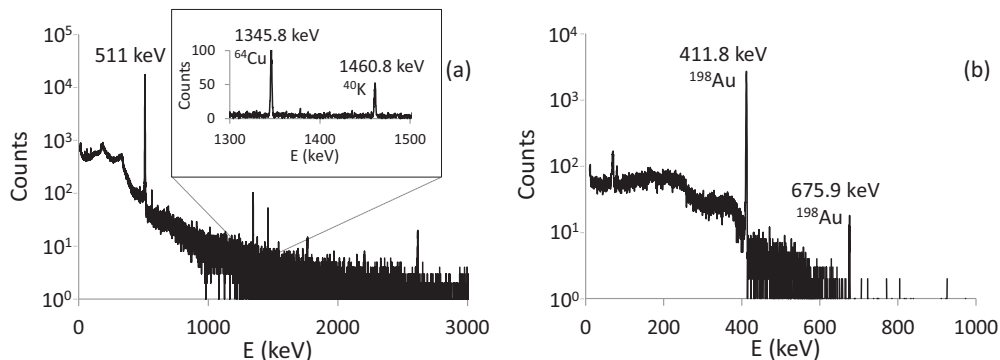
A small correction to the measured detection efficiency may be due to a slight difference between the ^{64}Cu and the ^{209}Pb decays or due to stronger β scattering within the lead foil. GEANT Monte Carlo simulations [21] were performed in order to evaluate this correction. The iSolo500 detector, sample geometry, and the initial β or positron energy were introduced into the simulation, and the spectra of the β energy spectra deposited in the detector were obtained for ^{64}Cu, ^{209}Pb, and ^{198}Au samples. Self-absorption of electrons and positrons, their backscattering in the detector, as well as interaction of γ rays with the detector material were taken into account. The samples' areal activity distribution measured by autoradiography (see below) was included into the simulations. The simulated response of the β detector for the three samples is shown in Fig. 3. The simulated spectra were generated for 10^7 decay events for each case. The spectra in Fig. 3 were normalized to compare the experimental results. The simulations reproduce well the main features of the experimental spectra. Some disagreement between the simulations and the experiment is observed for the very weak high-energy tails which probably are associated with summing in the detector of β- and γ-ray signals. Contribution of these tails in the spectra integral is negligible.

Integration of the simulated spectra above the 125-keV threshold leads to the simulated detection efficiency values of 20.8(10)%, 21.1(10)%, and 24.2(10)% for the ^{64}Cu, ^{209}Pb, and ^{198}Au isotopes. As seen from Table I the simulations underestimate the absolute experimental efficiencies measured for ^{64}Cu and ^{198}Au isotopes. This is probably due to the lack of complete knowledge on the iSolo detector geometry. Nevertheless the simulations verify the good choice of the ^{64}Cu decay for measuring β efficiency for the ^{209}Pb sample. The adopted value of β detection efficiency for the ^{209}Pb decay was taken as 25.6(1.3)%. A conservative 2% uncertainty obtained from the GEANT4 simulation was included in the experimental error. This result is not sensitive to the detection threshold. We have decided not to integrate the measurement and simulation of the ^{198}Au sample into the evaluation of ^{209}Pb β detection efficiency. Such an attempt would lead to additional systematic errors associated with uncertainty of the detection threshold.

As mentioned above, the gold targets were used for measurement of neutron fluence and distribution. The autoradiographic images of the foils were taken by placing them
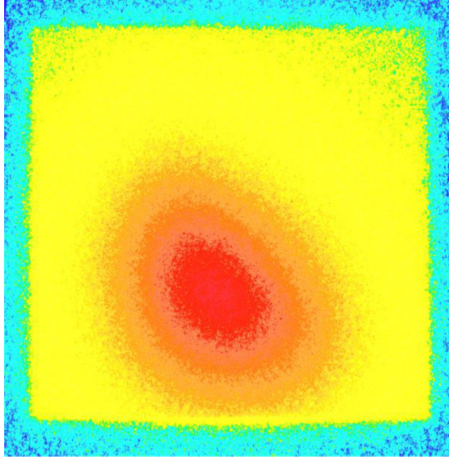

FIG. 4. (a) A γ spectrum taken with the copper sample. The 1345.8-keV γ ray is shown in the inset. (b) The γ spectrum of one of the gold samples.

FIG. 5. An autoradiograph of one of the gold samples. The yellow square corresponds to a 25×25 mm^2 gold foil and is centered on the ion-optical axis of the proton (and neutron) beam. The vertical color scale is linear.

after the decay of 3 weeks on a photographic FUJI image plate. The exposure time was 100 s. The activity distribution (Fig. 5) corresponds to the neutron flux distribution over the target area. As is seen in the figure, there was a 4-mm vertical shift of the cone distribution with respect to the target. Such offsets in the vertical direction were observed in previous LiLiT irradiations. Further improvement of beam diagnostics is required to resolve this experimental problem. The simulations (see below) showed that this offset did not lead to a significant effect on the experimental results.

IV. ANALYSIS AND RESULTS

A. Monte Carlo simulations

The Monte Carlo simulations performed with the codes SIMLIT-GEANT4 [22] include neutron production in the liquid-lithium target, neutron transport and scattering in the structural materials [21], and simultaneous calculations of the activities produced in the gold monitors and in the Pb target. The beam energy and energy spread as well as the proton beam transverse distribution on the lithium jet, geometrical position of the activation targets, and all surrounding material were introduced into the simulations. The measured offset between the neutron cone and the target position (Fig. 5) also was taken into account. The simulation indicates that the offset caused an approximately 1% reduction in the evaluated neutron yield. The calculations for the ^{197}Au$(n,\gamma)^{198}$Au reaction are performed using the ENDF/B-VII.1 cross-sectional evaluation [23]; the evaluation was checked carefully and found to be consistent with experimental data [14,15]. For ^{208}Pb, both ENDF/B-VII.1 and JENDL-4.0 [24] evaluations were used (see below). To measure the total neutron fluence the measured counting rate of the 411.8-keV γ was corrected for the detector efficiency, branching ratio, and decay losses in order to obtain the number of ^{198}Au nuclei produced in the irradiation. Comparison of this number with the simulation allowed obtaining the total neutron yield on the targets of $1.12(3) \times 10^{15}$, corresponding
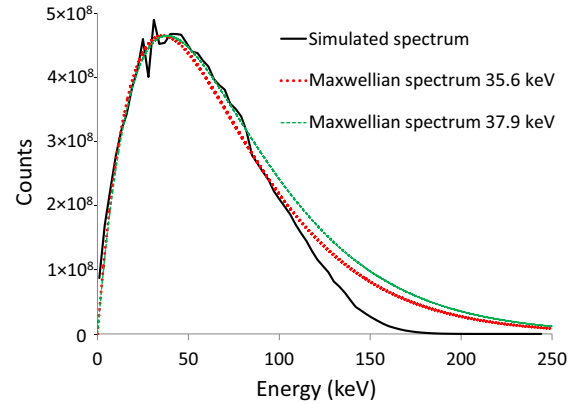

FIG. 6. A simulated neutron spectrum on the targets is compared with fitted MB distributions.

to $4.11(10) \times 10^{10}$ n/s/mA. The main experimental error was due to the Ge detector efficiency uncertainty ($\sim$2%) at 411.8 keV.

The simulations above allow us to derive also the integral neutron spectrum on the targets. The results of the simulations were verified in Refs. [12,25] where excellent agreement with angular differential and integral time-of-flight measurements was demonstrated. The simulated neutron energy spectrum is presented in Fig. 6. The simulations showed that spatial and energetic distributions were practically identical for all target foils. Some fine structure observed in the spectrum is due to neutron resonance processes in the surrounding materials mostly iron nuclei in stainless steel. The simulated spectrum dn_{sim}/dE_n cannot be fitted in the whole energy range by a Maxwell-Boltzmann (MB) distribution. Fitting over ranges of 0–80 and 0–120 keV is best fitted to a MB flux distribution ($E_n e^{-E_n/kT}$) with kT equal to 37.9 and 35.6 keV, respectively (Fig. 6).

B. Determination of the experimental cross section

The experimental ^{208}Pb$(n,\gamma)^{209}$Pb cross section σ_{exp}(Pb), averaged over the neutron energy distribution, is calculated by Eq. (1),

$$\sigma_{\text{exp}}(\text{Pb}) = \sigma_{\text{exp}}(\text{Au}) \frac{N_{^{209}\text{Pb}}}{N_{^{198}\text{Au}}} \frac{N_{\text{Au}}}{N_{\text{Pb}}} \frac{f_{^{198}\text{Au}}}{f_{^{209}\text{Pb}}}. \quad (1)$$

In this expression, σ_{exp}(Au) is the energy averaged ^{197}Au$(n,\gamma)^{198}$Au cross section (over the neutron energy distribution seen by the gold targets),

$$\sigma_{\text{exp}}(\text{Au}) = \int \sigma_{\text{ENDF}}(E_n, \text{Au}) \frac{dn_{\text{sim}}}{dE_n} dE_n \bigg/ \int \frac{dn_{\text{sim}}}{dE_n} dE_n. \quad (2)$$

Equation (2) yielded σ_{exp}(Au) of 537.1 and 536.2 mb for the upstream and downstream gold foils, respectively. Uncertainty in the evaluation of this cross section was estimated as 2%. For consistency the same cross section was evaluated using the JENDL library. The obtained values for the upstream and downstream foils are 535.3 and 534.5 mb correspondingly.

TABLE II. Summary of the experimental uncertainties.

Source of uncertainty	Group of errors	Uncertainty (%)
1345.8-keV peak statistical error	β detection efficiency	3.9
1345.8-keV Ge efficiency	β detection efficiency	2.7
Uncertainty from GEANT4 simulations	β detection efficiency	2
Error on nonpointlike source correction	β detection efficiency	1
Error on ^{64}Cu β and positron branching	β detection efficiency	1.4
Error on 1345.8-keV branching	β detection efficiency	0.7
^{64}Cu β and positron statistical errors	β detection efficiency	0.3
Uncertainty of σ_{lib}(Au) evaluation	Normalization to ^{198}Au	2
411.8-keV Ge efficiency	Normalization to ^{198}Au	2.0
411.8-keV peak statistical error	Normalization to ^{198}Au	0.65
Lead foil mass uncertainty	Number of Pb atoms	0.45
^{209}Pb β statistical error	β statistical error	0.2
Total error		6.5

$N_{\mathrm{Au}}(N_{\mathrm{Pb}})$ in Eq. (1) is the number of atoms in the gold (lead) target, $N_{^{198}\mathrm{Au}}(N_{^{209}\mathrm{Pb}})$ is the number of ^{198}Au(^{209}Pb) nuclei produced during the activation. $N_{^{198}\mathrm{Au}}$ was obtained from the measured intensity of the 411.8-keV transition (Fig. 4) corrected for the branching ratio, the Ge detector efficiency and decay loss. $N_{^{209}\mathrm{Pb}}$ was obtained by integration of the background corrected β spectrum from the lead sample (Fig. 3) using the measured β counting efficiency corrected for the abundance of the ^{208}Pb isotope and decay loss after irradiation. $f_{^{198}\mathrm{Au}}$ and $f_{^{209}\mathrm{Pb}}$ in Eq. (1) are factors reflecting the decay losses during the irradiation and after the irradiation for ^{198}Au and ^{209}Pb, respectively. Variation of the beam current and hence the neutron rate during the irradiation (Fig. 1) was taken into account in the calculations of $f_{^{198}\mathrm{Au}}$ and $f_{^{209}\mathrm{Pb}}$.

The obtained value of σ_{exp}(Pb) is 0.30(2) mb. The budget of experimental errors to the cross-sectional value is presented in Table II. The main contribution to the cross-sectional uncertainty is the statistical uncertainty in the 1345.8-keV photopeak yield and the uncertainty of the Ge detection efficiency of the ^{64}Cu line at 1345.8 keV at a 5-cm distance which was used for the determination of the efficiency of the iSolo500 β counter. The availability of a more advanced β detector, as for example, a 4π counter setup based on two Si(Li) detectors [6], would allow one to improve the experimental uncertainty of the present measurement by a factor of 2.

C. Determination of the ^{208}Pb$(n,\gamma)^{209}$Pb MACS cross section at 30 keV

The quasi-Maxwellian neutron energy spectrum used in irradiation differs from MB distribution (Fig. 6). Extrapolation

of the experimental cross section σ_{exp}(Pb) to the MACS cross section σ_{MACS}(Pb,kT) introduces some correction, which was made using the evaluated cross sections from nuclear libraries [23,24]. The MACS cross section is obtained from the experimental cross section from ratios of the integrations of the evaluated cross section σ_{lib}(Pb, E_n) over MB and simulated dn_{sim}/dE_n distributions [12],

$$\sigma_{\mathrm{MACS}}(\mathrm{Pb},kT) = \frac{2}{\sqrt{\pi}}\sigma_{\mathrm{exp}}(\mathrm{Pb})C_{\mathrm{lib}}(\mathrm{Pb},kT), \quad (3)$$

where

$$C_{\mathrm{lib}}(\mathrm{Pb},kT) = \frac{\int_0^\infty \sigma_{\mathrm{lib}}(\mathrm{Pb},E_n)E_n e^{-E_n/kT} dE_n}{\int_0^\infty E_n e^{-E_n/kT} dE_n}$$
$$\times \frac{\int_0^\infty \frac{dn_{\mathrm{sim}}}{dE_n} dE_n}{\int_0^\infty \sigma_{\mathrm{lib}}(\mathrm{Pb},E_n)\frac{dn_{\mathrm{sim}}}{dE_n} dE_n}. \quad (4)$$

Unlike the case of gold there are significant differences in the evaluation of the ^{208}Pb$(n,\gamma)^{209}$Pb cross section in different nuclear data libraries, leading to the differences in the C_{lib}(Pb,kT) factors. The results for σ_{MACS}(Pb), σ_{MACS}(Cu), and σ_{MACS}(Au), calculated for $kT = 30$ keV using the ENDF and JENDL libraries are presented in Table III. As is seen from the table the correction factors C_{lib}(Pb) differ by $\sim 7\%$ for the two libraries.

It is interesting to compare the ^{208}Pb$(n,\gamma)^{209}$Pb evaluations from the ENDF and JENDL nuclear libraries [26] with the experimental data from the literature. The striking difference between the evaluated excitation functions from the ENDF and JENDL libraries is shown in Fig. 7(a). The JENDL evaluation

TABLE III. The MACS cross section calculated from the experimental cross sections for two isotopes using the ENDF and JENDL nuclear libraries. All $C_{\mathrm{lib}}(A)$ and $\sigma_{\mathrm{MACS}}^{\mathrm{lib}}(A)$ values were calculated for $kT = 30$ keV.

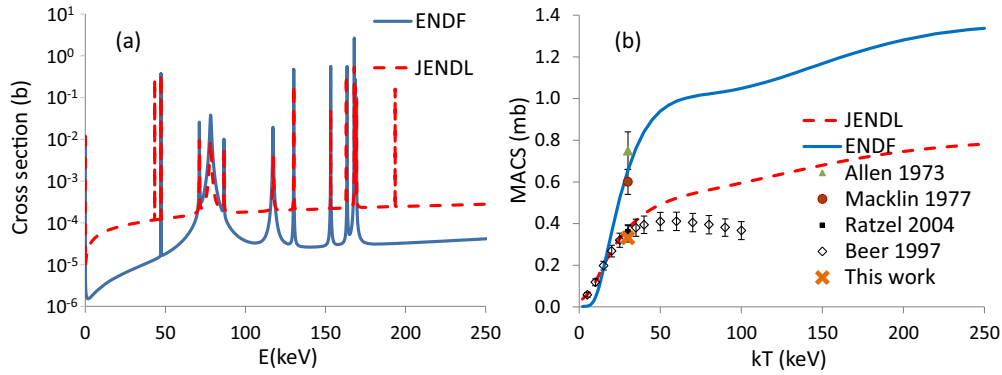| A	$\sigma_{\mathrm{exp}}(A)$ mb	$C_{\mathrm{ENDF}}(A)$	$C_{\mathrm{JENDL}}(A)$	$C_{\mathrm{JENDL}}(A)/C_{\mathrm{ENDF}}(A)$	$\sigma_{\mathrm{MACS}}^{\mathrm{ENDF}}(A)$ mb	$\sigma_{\mathrm{MACS}}^{\mathrm{JENDL}}(A)$ mb
^{208}Pb	0.30(2)	0.900	0.964	1.07	0.30(2)	0.33(2)
^{63}Cu	67.1(3.4)	1.049	1.030	0.98	70.4(3.4)	69.1(3.4)
^{197}Au	537(11)	1.017	1.015	1.00	615(12)	616(12)

FIG. 7. (a) The evaluation of the ^{208}Pb$(n,\gamma)^{209}$Pb excitation functions from the ENDF and JENDL libraries. (b) Comparison the MACS cross section calculated with the ENDF and JENDL evaluated cross sections with the experimental data taken from Ref. [29].

has much stronger DC contribution, whereas the ENDF one exhibits much stronger strength of the resonances. In particular the difference in the strength and width of the broad resonance at 77.85 keV may result in a large effect on the extrapolation of the experimental data to the MACS cross section. It is worthwhile to mention the result of measurement of the 77.85-keV resonance strength 250(60) meV in Ref. [6] was dramatically lower than that of an earlier measurement of 1076(41) meV [27]. It is possible that the most recent data on the reaction resonances were not included in the ENDF evaluation. The MACS cross sections calculated with the ENDF and JENDL evaluations are compared with the experimental data from the literature [6,8,27,28] in Fig. 7(b). As seen in the figure the MACS obtained using the JENDL library is in much better agreement with the recent measurements [6,8] including the present paper, whereas the MACS obtained with the ENDF evaluation is in agreement with earlier experiments [27,28]. We use these observations to justify the adaptation of the correction from JENDL for the calculation of σ_{MACS}(Pb) (Table III). The final result of the present measurement for the MACS of ^{209}Pb at 30 keV is 0.33(2) mb, also plotted in Fig. 7.

D. Evaluation of the ^{63}Cu$(n,\gamma)^{64}$Cu MACS cross section at 30 keV

The ^{63}Cu$(n,\gamma)^{64}$Cu MACS cross section was obtained as a byproduct in this paper. Equation (2) was used for the calculation of σ_{exp}(Cu) (Table III). The number of ^{64}Cu atoms $N_{^{64}\mathrm{Cu}}$ was determined directly from integration of the 1345.8-keV γ peak corrected for the Ge detector efficiency, branching ratio, and correction associated with the size of the sample. The experimental errors are similar to those presented in Table II without contributions of the uncertainties related to measurement of β and positrons and with additional contribution of uncertainty of the copper foil thickness. The resulting experimental error is 5.3%. This error could readily be reduced by 30% if a thicker copper target was used in the experiment. Equation (3) was employed to obtain the σ_{MACS}(Cu) value (Table III). The factor C_{lib}(Cu) is not very sensitive to the choice of the nuclear library. We adopt the value for σ_{MACS}(Cu) of 69.7(3.4)(1) mb, the average between the ENDF and the JENDL results. The second error is the uncertainty of choice of the nuclear library.

V. DISCUSSION

The ^{208}Pb$(n,\gamma)^{209}$Pb MACS cross sections at 30 keV were measured to be 0.33(2) mb. We argue that the JENDL library is the better choice for the evaluation of the MACS cross section from the experimental data. In the case when both the JENDL and the ENDF libraries are used for evaluation the adopted value should be 0.315(20)(22) mb where the second parenthesis is the systematic uncertainty associated with the libraries' disagreement. The result of the present paper is compared with the literature [5,6,8,27,28] in Fig. 8. As can be seen in the figure the present paper is in good agreement with both the most recent TOF [6] and the activation [5,8] measurements. This indicates that the calculated theoretical DC cross-sectional contribution in the TOF measurement is acceptable. It is interesting to compare, in more detail, the present experiment with Ref. [8]. Both experiments utilize the same technique for the production of quasi-Maxwellian neutron spectra. Although our experiment utilized a much more intense neutron source, a superior β detection system was used in Ref. [8]. The MACS cross section for $kT = 25$ keV was quoted as 0.30(2) mb in Ref. [8]. This was evaluated to be 0.36(3) mb for 30 keV in Ref. [29], which is in good agreement with our result of 0.33(2) mb. The good agreement between the two activation measurements performed at very different conditions at the Karlsruhe Van de Graaf and at the SARAF
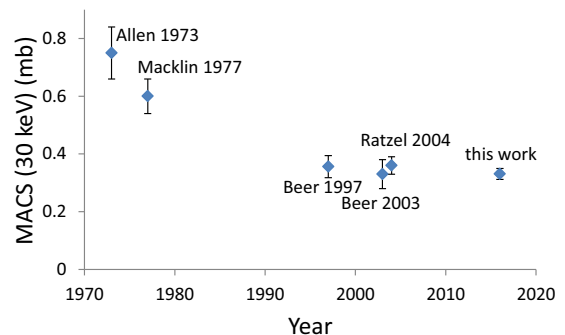

FIG. 8. Summary of the MACS ^{208}Pb$(n,\gamma)^{209}$Pb cross-sectional values at 30 keV taken from Ref. [29]. The error bar for Ratzel [8] is taken from Ref. [29]. The original experimental error for 25 keV was 0.02 mb, see Ratzel [8].

linear accelerators indicates good control on systematic uncertainties.

The present paper supports the main astrophysical conclusions regarding *s*-process termination [5,6,8]. The *s*-process reaction flow is trapped by the very small ^{208}Pb cross section and, to a large extent, the *s* process is terminated at ^{208}Pb. As a consequence the abundance of the ^{209}Bi isotope is mostly due to *r*-process contribution.

The resulting ^{63}Cu$(n,\gamma)^{64}$Cu MACS cross sections at 30 keV and 69.7(3.4)(1) mb can be compared with the recommended value from the previous experiments [29], 55.7 mb, and the results of the recent work [30], 84.0(1.1)(6.7) mb, showing that a further experimental determination of this cross section is necessary.

In conclusion, the very small ^{208}Pb$(n,\gamma)^{209}$Pb MACS cross section was remeasured at SARAF Phase I with the LiLiT target and a 1.5-mA CW proton beam. The result agrees with the latest measurements and confirms the main astrophysical conclusions of the earlier studies. Good agreement between the present MACS ^{208}Pb$(n,\gamma)^{209}$Pb result and the earlier Karlsruhe experiment raises confidence in the method of stellar reaction measurements via activation with quasi-Maxwellian neutron sources.

[1] F. Kappeler, R. Gallino, S. Bisterzo, and W. Aoki, Rev. Mod. Phys. **83**, 157 (2011)

[2] D. Clayton and M. Rassbach, Astrophys. J. **148**, 69 (1967).

[3] S. Bisterzo, R. Gallino, O. Straniero, S. Cristallo, and F. Kappeler, Mon. Not. R. Astron. Soc. **418**, 284 (2011).

[4] L. J. Shingles, A. I. Karakas, R. Hirschi, C. K. Fishlock, D. Yong, G. S. Da Costa, and A. F. Marino, Astophys. J. **795**, 34 (2014).

[5] H. Beer, W. Rochow, F. Kappeler, and T. Rauscher, Nucl. Phys. A **718**, 518 (2003).

[6] H. Beer, F. Corvi, and P. Mutti, Astrophys. J. **474**, 843 (1997).

[7] W. Ratynski and F. Kappeler, Phys. Rev. C **37**, 595 (1988).

[8] U. Ratzel, C. Arlandini, F. Käppeler, A. Couture, M. Wiescher, R. Reifarth, R. Gallino, A. Mengoni, and C. Travaglio, Phys. Rev. C **70**, 065803 (2004).

[9] S. Halfon *et al.*, Rev. Sci. Instrum. **84**, 123507 (2013).

[10] S. Halfon *et al.*, Rev. Sci. Instrum. **85**, 056105 (2014).

[11] A. Kreisel *et al.*, in *LINAC14: Proceedings of the 27th International Linear Accelerator Conference, Geneva, 2014*, edited by C. Carli, M. Draper, Y.-M. Ducimetiere, A. McCausey, R. Müller, J. Poole, and V. R. W. Schaa (CERN, Meyrin, Canton of Geneva, 2014), paper WEIOB02, p. 770.

[12] M. Tessler *et al.*, Phys. Lett. B **751**, 418 (2015).

[13] http://www.goodfellow.com

[14] C. Lederer *et al.* (n_TOF Collaboration), Phys. Rev. C **83**, 034608 (2011).

[15] C. Massimi *et al.*, Eur. Phys. J. A **50**, 124 (2014).

[16] http://lebowcompany.com

[17] L. Weissman *et al.*, J. Instrum. **10**, T10004 (2015).

[18] http://www.canberra.com/products/radiochemistry_lab/pdf/iSolo-SS-C39505.pdf

[19] M.-M. Be *et al.*, Appl. Radiat. Isot. **70**, 1894 (2012).

[20] http://www.gespecor.de

[21] S. Agostinelli *et al.*, Nucl. Instrum. Methods Phys. Res., Sect. A **506**, 250 (2003).

[22] M. Friedman *et al.*, Nucl. Instrum. Methods Phys. Res., Sect. A **698**, 117 (2013).

[23] M. B. Chadwick *et al.*, Nucl. Data Sheets **112**, 2887 (2011).

[24] K. Shibata *et al.*, J. Nucl. Sci. Technol. **48**, 1 (2011).

[25] G. Feinberg, M. Friedman, A. Krása, A. Shor, Y. Eisen, D. Berkovits, D. Cohen, G. Giorginis, T. Hirsh, M. Paul, A. J. M. Plompen, and E. Tsuk, Phys. Rev. C **85**, 055810 (2012).

[26] http://www.nndc.bnl.gov

[27] R. L. Macklin, J. Halperin, and R. R. Winters, Astrophys. J. **217**, 222 (1977).

[28] B. Allen, R. Macklin, R. Winters, and C. Fu, Phys. Rev. C **8**, 1504 (1973).

[29] http://www.kadonis.org

[30] M. Weigand, C. Beinrucker, A. Couture, S. Fiebiger, M. Fonseca, K. Göbel, M. Heftrich, T. Heftrich, M. Jandel, F. Kappeler, A. Krása, C. Lederer, H. Y. Lee, R. Plag, A. Plompen, R. Reifarth, S. Schmidt, K. Sonnabend, and J. L. Ullmann, Phys. Rev. C **95**, 015808 (2017).